

Printability of 316 stainless steel

T. Mukherjee & T. DebRoy

To cite this article: T. Mukherjee & T. DebRoy (2019): Printability of 316 stainless steel, Science and Technology of Welding and Joining, DOI: [10.1080/13621718.2019.1607061](https://doi.org/10.1080/13621718.2019.1607061)

To link to this article: <https://doi.org/10.1080/13621718.2019.1607061>

 View supplementary material [↗](#)

 Published online: 18 Apr 2019.

 Submit your article to this journal [↗](#)

 View Crossmark data [↗](#)



Printability of 316 stainless steel

T. Mukherjee  and T. DebRoy

Department of Materials Science and Engineering, The Pennsylvania State University, University Park, PA, USA

ABSTRACT

A printability database can help in the selection of a printing process-alloy combination to reduce, and in some cases avoid, common defects in printed parts. The extensive testing of parts is not a viable option for determining printability because printing processes are inherently slow and expensive. Here we evaluate printability of stainless steel 316 by evaluating its susceptibilities to residual stresses, distortion, composition change and lack of fusion defects for laser (DED-L) and arc (DED-GMA) based directed energy deposition and laser powder bed fusion (PBF-L) processes using well-tested mechanistic models. Among these three processes, DED-GMA makes printed parts of 316 stainless steels most susceptible to residual stresses and distortion. High depth of penetration during DED-GMA makes components least susceptible to lack of fusion defects. Loss of volatile alloying elements from the tiny pools in PBF-L makes deposits the most vulnerable to composition change.

ARTICLE HISTORY

Received 17 December 2018
Revised 4 April 2019
Accepted 8 April 2019

KEYWORDS

Directed energy deposition; wire arc additive manufacturing; powder bed fusion; heat transfer and fluid flow; residual stresses; distortion; alloying element vaporisation; lack of fusion defect

Introduction

In the practice of welding, the widely used database of weldability [1] indicates if a welding process is recommended, difficult or cannot be easily undertaken for a given alloy. In the allied field of 3D printing, a similar concept of printability is still developing and currently there is no universally accepted definition for this term. In this paper, we use the word printability to mean the relative ease of converting an alloy feed stock to a sound part for a given combination of an alloy and a 3D printing process [2]. Recently, we evaluated [3] printability of different alloys for a given 3D printing process. However, printability of any alloy for all the commonly used printing processes is yet to be evaluated.

Three commonly used metal printing processes, directed energy deposition (DED) with gas-metal-arc (DED-GMA), DED-laser (DED-L), and powder bed fusion using a laser heat source (PBF-L) are operated using a wide variety of heat source power, scanning speed, layer thickness and mass deposition rate [2]. Based on the literature data [4–18] on printing of SS 316, Figure 1(a) shows that the arc power in DED-GMA can be 5–10 times higher than that of laser in DED-L and PBF-L. In contrast, the scanning speed in PBF-L can be 80–100 times faster than the other two processes. From Figure 1(b), it is evident that the faster deposition rate in DED-GMA is contributed by depositing layers of higher thicknesses, often 2–3 times thicker than that in DED-L. The PBF-L components are printed with thin layers that are 10–50 times thinner than those used in

DED-L and DED-GMA. Because of these variations, an alloy may experience a wide variation of cooling rate, temperature gradient, solidification rate and the resulting microstructure, defects and properties, depending on the printing process and the process parameters [2]. Currently, there is no generally available methodology to select an optimum printing process for a given alloy. Furthermore, the quality of the printed products made with various alloy-process combinations cannot be anticipated a priori. For the printing of a given alloy, the susceptibilities to common printing defects such as lack of fusion [19], compositional change [20], residual stresses [2] and distortion [3] are not known. Development of a printability [3] database will facilitate the selection of a printing process for an alloy and may be helpful to reduce common defects without any extensive trial and error testing.

Several attempts have been made to compare the susceptibilities of a particular alloy to these defects for different printing techniques. For example, Szost et al. [21] found that titanium alloy parts accumulate higher residual stresses when printed by the DED-GMA process compared with the DED-L process. Yang et al. [22] concluded that the ability of nickel alloy components to resist defects can vary depending on the process conditions. However, these findings do not provide any scales for comparing the relative susceptibilities of different printing processes to common printing defects. What is needed and not currently available is a ranking of printability of a particular alloy for different printing

CONTACT T. Mukherjee  tuhiniitb@gmail.com  Department of Materials Science and Engineering, The Pennsylvania State University, University Park, PA 16802, USA

 Supplemental data for this article can be accessed here. <https://doi.org/10.1080/13621718.2019.1607061>

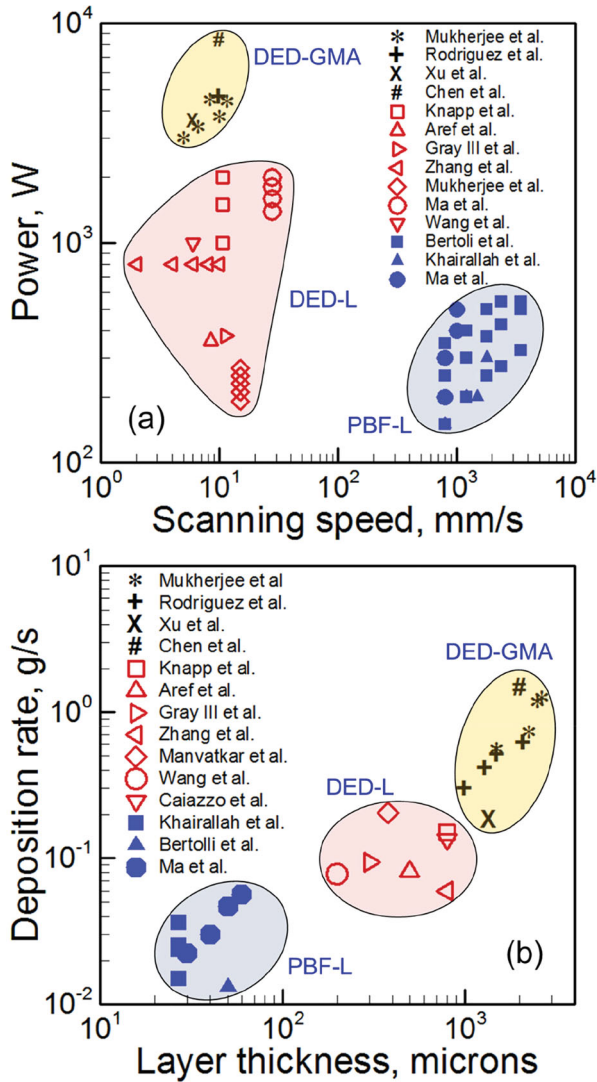


Figure 1. Variations of (a) heat source power and scanning speed and (b) mass deposition rate and layer thickness for PBF-L, DED-L and DED-GMA processes for 316 stainless steel [4–18]. The curved lines for each process show regions that contain all data points.

processes by comparing relative susceptibilities of the printed parts to common defects.

Extensive testing of specimens is routinely used in the field of welding to determine weldability. However, experiments alone do not provide a viable path for determining printability because of the following compelling reasons. First, parts are often printed by the deposition of thin metal layers, often thinner than a human hair [2]. As a result, it often takes a day or more to prepare a single sample. Therefore, it would be practically impossible to prepare the same number of printed samples as needed for weldability testing in a given time. Second and more important, the costs of printing equipment and feed stock materials are significantly higher than those in welding [2]. As a result, the costs of preparing the necessary matrix of specimens for three printing process variants would be prohibitive. Therefore, a recourse is to follow a new path that is reproducible and verifiable through the use of

well-tested numerical models of metal printing. Here we rank the printability or the relative susceptibilities of 316 stainless steel (SS 316) parts to residual stresses, distortion, composition change and lack of fusion for DED-GMA, DED-L and PBF-L processes using well-tested heat transfer and fluid flow calculations and thermomechanical simulations.

Calculation of printability

Heat transfer and fluid flow calculations

The processing conditions for the three printing processes used to calculate the printability by estimating residual stresses, distortion, composition change and lack of fusion defect are adapted from the literature [4,5,23] and are reported in Table 1. Estimation of all four defects requires accurate calculations of three-dimensional, transient temperature fields and molten pool shape and size. For this purpose, well-tested heat transfer and fluid flow models of PBF-L [24], DED-L [5] and DED-GMA [25] are used. The governing equations and boundary conditions are described in details in our previous publications [5,17,24–26] and are not repeated here. Thermo-physical properties [27] of SS 316 used for the calculations are provided in the Supplementary information.

Residual stresses and distortion

Based on the transient, three-dimensional temperature field, residual stresses are calculated using a well-tested, finite element based thermo-mechanical model [28–29]. Mechanical properties of SS 316 used for the calculations are provided in the Supplementary information. The effects of solid state phase transformation of SS 316 on residual stresses are neglected for simplicity. For consistency, geometry of the solution domain for the three processes is considered to be identical. It consists of a 16 mm long and 4 mm high thin wall built on a 20 mm long and 10 mm thick substrate. However, the thin wall is made of multiple layers using PBF-L, DED-L and DED-GMA processes depending on the layer thicknesses (Table 1). The surfaces of the thin wall are assumed to be flat in the thermo-mechanical

Table 1. Process parameters used for evaluating printability.

| Process parameters | DED-GMA [4] | DED-L [5] | PBF-L [23] |
|--------------------------|-------------|-----------|------------|
| Laser power (W) | | 1500 | 110 |
| Arc current (A) | 150 | | |
| Arc voltage (V) | 14.2 | | |
| Heat source power (W) | 2130 | 1500 | 110 |
| Scanning speed (mm/s) | 10 | 10.6 | 100 |
| Layer thickness (mm) | 1.0 | 0.8 | 0.25 |
| Wire radius (mm) | 0.5 | | |
| Wire feed rate (m/min) | 8.0 | | |
| Catchment efficiency | | 0.3 | |
| Deposition rate (g/s) | 0.5 | 0.2 | |
| Heat source radius (mm) | 4.0 | 2.0 | 0.3 |
| Substrate thickness (mm) | 10.0 | 12.7 | 0.75 |

model for simplicity. The calculations are performed in Cartesian coordinate system (x , y and z). The mechanical boundary condition is applied by constraining the bottom surface of the substrate.

To quantify the distortion during printing, we have used a recently proposed a non-dimensional strain parameter [3],

$$\varepsilon^* = \frac{\beta \Delta T}{EI} \frac{t}{F\sqrt{\rho}} H^{3/2} \quad (1)$$

where β is the co-efficient of volumetric expansion and ΔT is the difference between the peak temperature and solidus temperature, t is the total building time, H is the heat input per unit length of the build, EI is the flexural rigidity of the substrate, F is the Fourier number [6] and ρ is the density of alloy. Peak temperature and pool length on which the Fourier number depends are calculated using the heat transfer and fluid flow model. An example of the distortion calculation is provided in the Supplementary information.

Composition change

Composition change depends on the rates of vaporisation of different alloying elements [3] from the top surface of the molten pool and the geometry of the fusion zone. Vaporisation rates are calculated using a model proposed by Knight [30] using the top surface temperature of the molten pool which is calculated using the heat transfer fluid flow models. The detail procedure for calculating composition change due to evaporative loss from a molten pool can be found elsewhere [31] and is not repeated here. An example of the composition change calculation is provided in the Supplementary information.

Lack of fusion defects

Detailed calculations of lack of fusion defect is provided in recent literature [19]. Insufficient overlap of the fusion zone with both the adjacent track and the previously deposited layer below is a major contributing factor for this type of defects. Based on the analysis of the available experimental data, it has been shown that a ratio of molten pool depth to layer thickness correlates well with the occurrence of lack of fusion defects in thin wall builds [3]. Therefore, this index, which can be computed from numerical heat transfer models, is used as a relative measure of estimating the propensity of lack of fusion defects.

Model validations

Fusion zone geometry

Figure 2 shows that the calculated shape and size of the transverse (YZ plane) section of single track SS 316

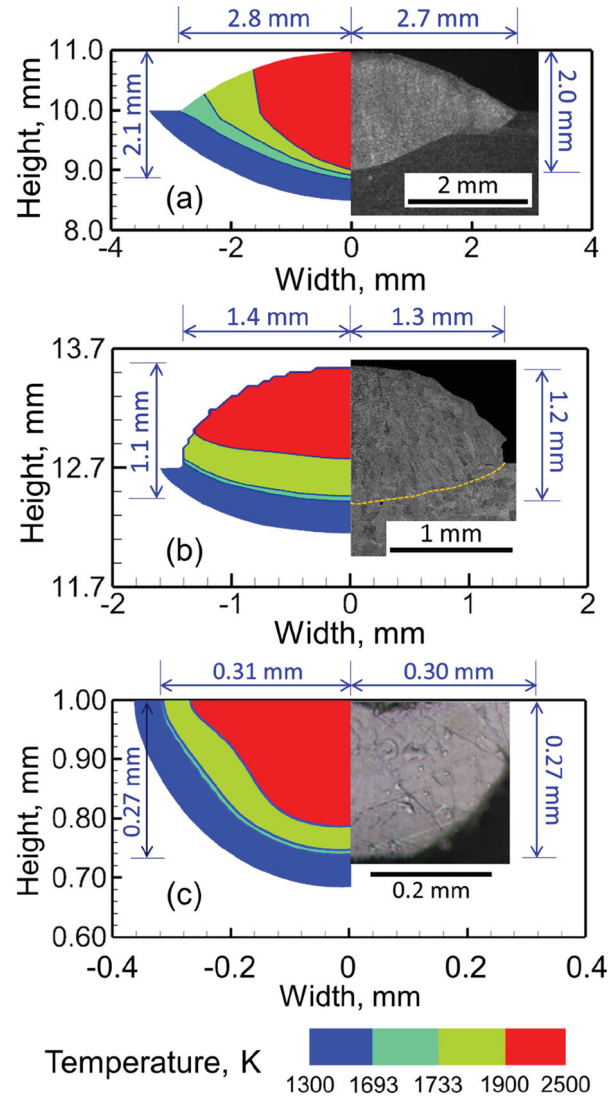


Figure 2. Comparison between the calculated transverse sections of the deposit with the corresponding experimental results [4,5,23] for (a) DED-GMA, (b) DED-L and (c) PBF-L. The process conditions are given in Table 1. The width and depth of the deposits are provided to clearly indicate the size differences.

builds printed using three processes agree well with the corresponding experimental results [4,5,23]. The molten pool is bounded by the solidus temperature (1693 K). The shape and size of the curved surface of the DED-GMA deposit are determined by the combined effects of arc pressure, surface tension of the liquid metal and volume of the molten droplets [25]. The impingement of the droplets also results in deep penetration in DED-GMA [25], as shown in Figure 2(a). However, in DED-L the curved pool surface is formed immediately under the laser beam due to the addition of powder particles [5], as shown in Figure 2(b). In contrast, Figure 2(c) shows that the top surface of the PBF-L build is flat because of the addition of thin layers of powders during printing [24]. The linear heat input (power/speed) in PBF-L is the lowest of the three processes, of the order of 0.1 J/mm, which results in very small pool whose length, width and depth are

measured in micrometers. However, the linear heat inputs in DED-L and DED-GMA are in the order of 10 and 100 J/mm, respectively. Therefore, the molten pool dimensions in DED-GMA are larger than those in DED-L. Figure 2 shows that the pool dimensions in PBF-L are approximately 10% of DED-GMA and 30% of DED-L. The results in Figure 2 show that the numerical models of the three processes are capable of correctly predicting the widely different fusion zone geometries in each case.

Residual stresses and distortion

To validate the thermo-mechanical model used here, calculated stresses are compared with the corresponding experimental data [32] for 10 layers stainless steel 410 components printed using DED-L at two different heat inputs. Thermo-mechanical behaviour of this stainless steel is similar to that of stainless steel 316 and the property data used in the calculations are taken from the literature [29]. Numerically computed

through-thickness residual stress (σ_{zz}) profiles along both deposition and build directions agree well with corresponding experimental results [32] as shown in Figure 3(a,b) respectively.

Composition change

Calculated changes in composition of four main constituting elements of stainless steel agree well with the corresponding experimental data [33] for DED-L as shown in Figure 3(c). Experimentally measured values of compositions in the alloy powders and the built specimens were reported. Composition change is estimated based on those reported values. The computed composition change values agree well with the corresponding experimental data.

Lack of fusion defects

Since the available experimental data show that the extent of lack of fusion defects scales well with the

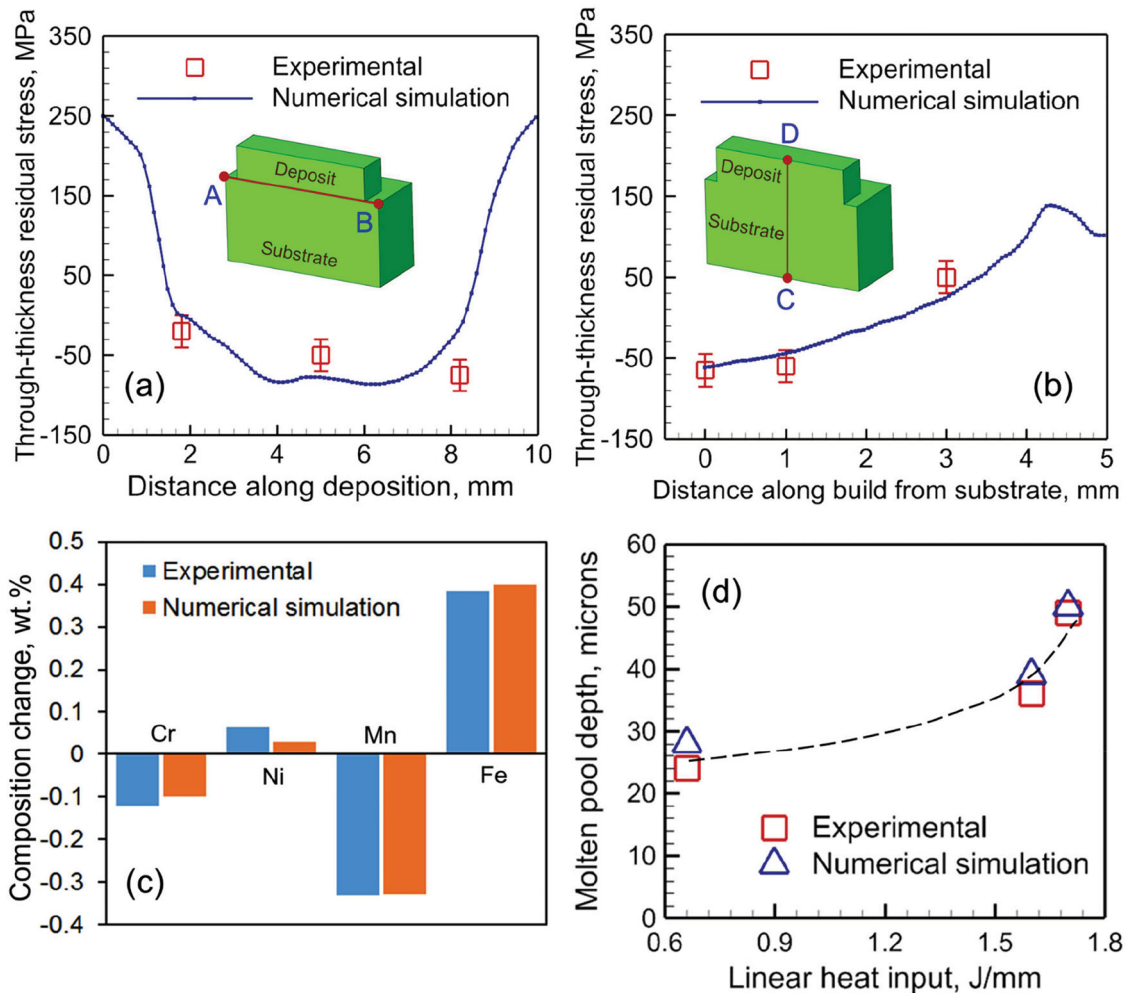


Figure 3. Comparison between the experimentally measured [32] and numerically computed through-thickness residual stress profiles during DED-L along (a) horizontal deposition direction from A to B in the mid-width of the build and (b) vertical build direction from C to D in the mid-width of the build. Laser power for figure (a) and (b) are 300 and 600 W respectively. Other processing conditions are available in the corresponding literature [32]. (c) Comparison between the experimentally measured [33] and numerically computed composition change for four main constituting elements of stainless steel during DED-L. Processing conditions are available in the corresponding literature [33]. (d) Comparison between the experimentally measured [34] and numerically computed pool depth during PBF-L of stainless steel 316. Processing conditions are available in the corresponding literature [34].

geometry of the fusion zone, specifically with the ratio of the pool depth to layer thickness, this ratio was used to estimate susceptibility to lack of fusion defect. For a given printing process, if the layer thickness is known, the pool depth can be computed from the numerical heat transfer and fluid flow model. Figure 3(d) compares the numerically computed pool depth with the corresponding experimental data [34] during PBF-L of stainless steel 316. Very good agreement between the experimental and calculated results provides us confidence to use these models for evaluating lack of fusion defects.

Results and discussions

Residual stresses and distortion

Figures 4(a–c) show the computed longitudinal stress (x -component, σ_{xx} , i.e. along the scanning direction) distribution in the SS 316 components printed using the three processes. The wall printed using DED-GMA is the widest because of the biggest molten pool of this process (Figure 2). In addition, DED-GMA components are printed using the thickest layers among the three processes (Table 1). Thick and wide tracks accumulate high residual stresses during cooling [28] and makes the DED-GMA component the most vulnerable to residual stresses among the three printing processes as shown in Figure 4(a). The calculated values of residual stresses are in the same order of magnitude with the reported values in the literature [35] on DED-GMA of steel. Because of the tiny molten pool and thinnest layers in PBF-L, the component printed using this process accumulates the least residual stresses as shown in Figure 4(c). The variations in longitudinal stresses at different transverse sections (YZ planes) along the length of the deposit are shown in the Supplementary information. The three processes also exhibit the same trend for the susceptibility to the through-thickness (σ_{zz} , i.e. along z -direction) residual stress and the corresponding results are provided in the Supplementary information.

Accumulation of high residual stresses along the substrate deposit interface may result in detachment of the part from the substrate [28]. Therefore, in Figure 5(a), the computed longitudinal residual stresses along the substrate deposit interface (AB) for the SS 316 components printed using three processes are compared. Cooling of the largest fusion zone in DED-GMA results in the accumulation of high tensile stress along the substrate deposit interface as shown in Figure 5(a). In contrast, the components printed using PBF-L accumulates the least residual stresses along the substrate deposit interface because it has the smallest fusion zone of the three printing processes.

To provide a quantitative scale for evaluating the relative susceptibilities of DED-GMA, DED-L and PBF-L

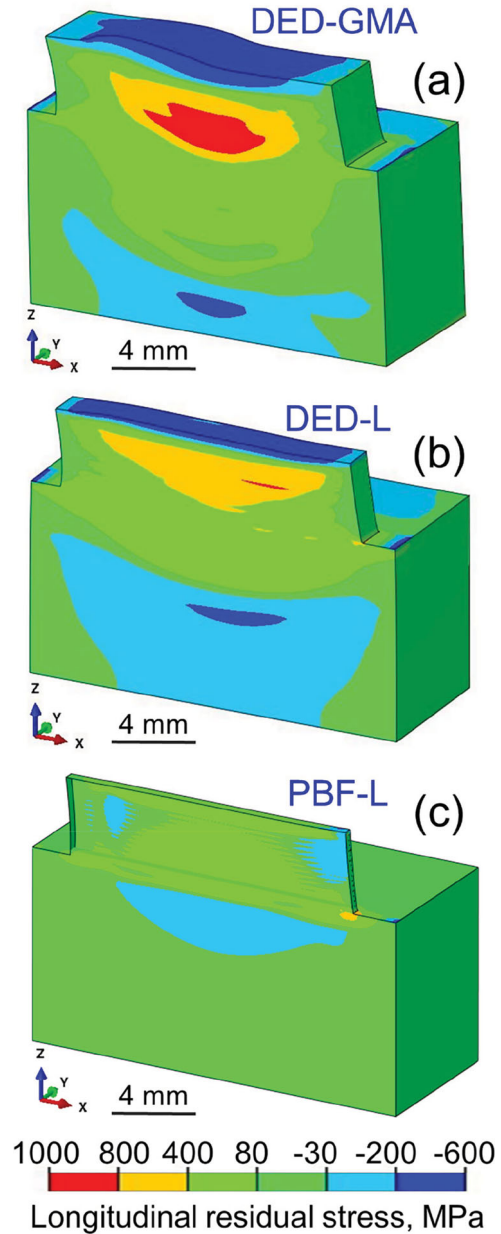


Figure 4. Longitudinal residual stress distribution in a SS 316 deposit printed using (a) DED-GMA (b) DED-L and (c) PBF-L. The process conditions are given in Table 1. For consistency, all parts are 16 mm long, 4 mm high and built on a 20 mm long, 10 mm wide and 10 mm thick substrate. The three parts are printed using 4, 5 and 16 layers for DED-GMA, DED-L and PBF-L, respectively due to the difference in the layer thicknesses of these processes. The scanning direction is along the positive x -axis. Half of the solution domain is shown because of the symmetry with respect to XZ plane.

to distortion, Figure 5(b) compares the values of strain parameter which is a measure of distortion (Equation (1)) while depositing the 1st layer of SS 316 deposits printed using the three processes. The figure shows that the molten pool in DED-GMA is significantly larger than those for DED-L and PBF-L respectively. Shrinkage of large pools during solidification makes the DED-GMA components are the most susceptible to distortion among the three printing processes.

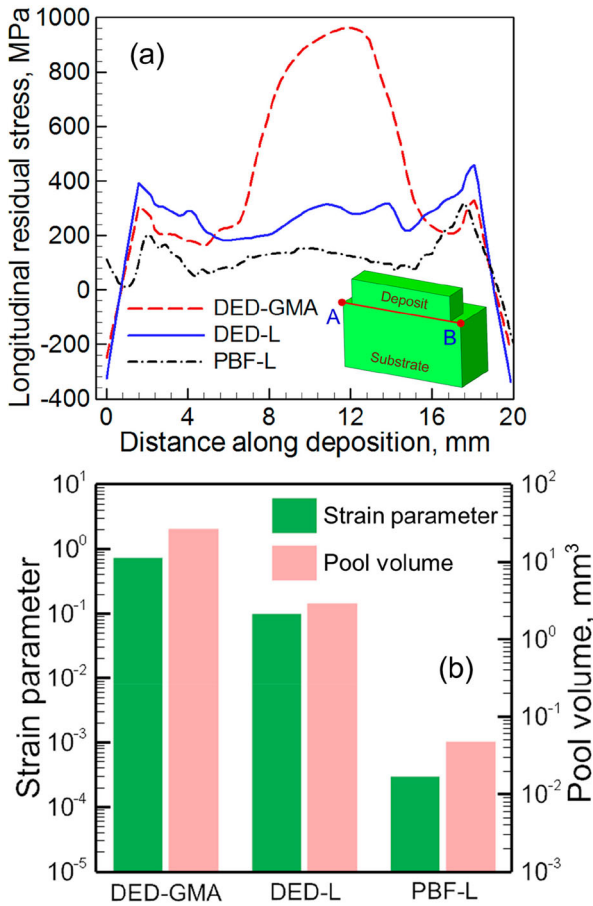


Figure 5. (a) Longitudinal residual stress distribution for DED-GMA, DED-L and PBF-L along substrate-deposit interface (AB, where A = 0 mm and B = 20 mm). The scanning direction is along the positive x-axis (refer Figure 4). (b) Strain parameters and maximum pool volume while depositing the 1st layer of SS 316 deposits using the three printing techniques. The process conditions are given in Table 1. Same substrate dimensions (20 mm long, 10 mm wide, 10 mm thick) are taken for all three cases for consistency.

Composition change

As reported in the literature [3] and also observed in our analysis (see the Supplementary information for the results), manganese is the most susceptible element for composition change among all constituting elements of SS 316. Figure 6(a) compares the percentage change in manganese in single track SS 316 deposits printed using the three processes. As well-established in the welding literature [31], susceptibilities to composition change depends on both the vaporisation rate and the ratio of the top surface area to volume of the fusion zone. The amount of mass loss due to evaporation is proportional to the surface area of the fusion zone. However, loss of alloying elements from a smaller molten pool results in a more pronounced change in composition. Because of the smallest volume of molten pool in PBF-L among the three processes, the value of the ratio is significantly higher than those for DED-L and DED-GMA. As a result, PBF-L components are more susceptible to composition change than the other

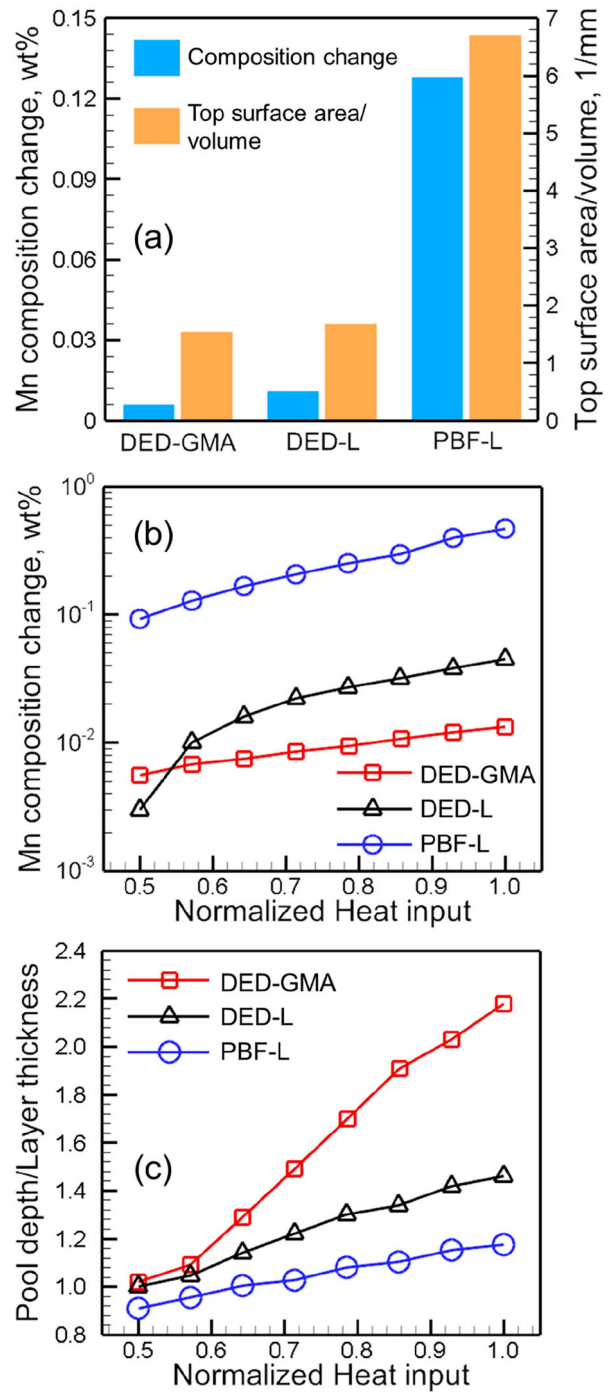


Figure 6. (a) Change in manganese composition and the ratio of the top surface area to volume of the fusion zone for a single track SS 316 component printed using three printing techniques. The process conditions are given in Table 1. (b) Variations in manganese composition of SS 316 builds printed using the three techniques. The normalised heat input refers to the ratio of heat input to the maximum heat input for the printing process. In both figures (a) and (b) composition change refers to reduction in its concentration. (c) Variations in pool depth to layer thickness ratio (an indicator of lack of fusion defect) of SS 316 builds printed using three techniques. All process variables are presented in Table 1. The laser power and speed are varied in figures (b) and (c).

two processes as shown in Figure 6(a). Figure 6(b) also indicates that the SS 316 component printed using PBF-L is the most susceptible to composition change for a

wide range of linear heat input among all three printing processes.

Lack of fusion defects

In order for a deposited layer to bond properly with a previously deposited layer, the depth of the molten pool should exceed the layer thickness considerably. Therefore, the higher the value of the ratio of depth of penetration to the layer thickness, the better the fusional bonding between the layers. Figure 6(c) evaluates the relative susceptibilities to lack of fusion defect of the three printing processes by comparing the corresponding values of the ratio of the pool depth to layer thickness. For all three processes, pool depth increases with the heat input and ensures better fusional bonding among layers. However, deep penetration of the molten pool in the DED-GMA due to the impingement of molten droplets makes this process the least susceptible to lack of fusion defect.

Summary and conclusions

Printability of stainless steel 316 (SS 316) for DED-L, DED-GMA and PBF-L has been quantitatively evaluated by comparing the relative susceptibilities of residual stresses, distortion, composition change and lack of fusion defect using well-tested heat transfer fluid flow model and the literature data. The results are summarised in Table 2. Below are the specific findings.

- (1) High deposition rate of DED-GMA allows fabrication of the component using thicker layers than DED-L and PBF-L. Deposition of thick layers results in accumulation of the highest residual stresses in DED-GMA components among the three processes. For example, the longitudinal residual stress in DED-GMA component can be around 6 times higher than that in PBF-L component that is printed with layers 4 times thinner than that for DED-GMA.
- (2) Rapid scanning speed of PBF-L results in a molten pool that has higher liquid pool free surface to volume ratio than those for DED-L and DED-GMA. Therefore, more materials vaporise per unit volume of the molten pool and make PBF-L components the most susceptible to composition change.

Table 2. Comparison of relative susceptibilities of SS 316 components printed using the three printing techniques to the defects. The values are for the processing conditions in Table 1.

| Process parameters | DED-GMA | DED-L | PBF-L |
|---|---------|-------|--------|
| Maximum longitudinal residual stress at the substrate deposit interface (MPa) | 950 | 450 | 150 |
| Strain parameter | 0.70 | 0.09 | 0.0003 |
| Mn composition change, wt-% | 0.0060 | 0.011 | 0.128 |
| Pool depth/layer thickness | 1.30 | 1.14 | 1.08 |

Depending on the processing conditions, percentage change in the manganese content in SS 316 component printed using PBF-L can be significantly higher than those in DED-L and DED-GMA components.

- (3) Deep penetration of the molten pool in DED-GMA due to the droplet impingement ensures sound bonding with the previously deposited layers. Therefore, DED-GMA component is the least vulnerable to the lack of fusion defect among the three printing processes.
- (4) The typical molten pool size in DED-GMA is significantly larger than those for DED-L and PBF-L. Larger molten pool shrinks more during solidification and makes the DED-GMA component vulnerable to thermal distortion. Therefore, DED-GMA components have the most susceptibility to distortion among the three printing processes considered here.

Disclosure statement

No potential conflict of interest was reported by the authors.

ORCID

T. Mukherjee  <http://orcid.org/0000-0001-5372-4887>

References

- [1] Lippold JC. *Welding metallurgy and weldability*. Hoboken (NJ): Wiley; 2014.
- [2] DebRoy T, Wei HL, Zuback JS, et al. Additive manufacturing of metallic components – process, structure and properties. *Prog Mater Sci*. 2018;92:112–224.
- [3] Mukherjee T, Zuback JS, De A, et al. Printability of alloys for additive manufacturing. *Sci Rep*. 2016;6:19717.
- [4] Rodriguez N, Vázquez L, Huarte I, et al. Wire and arc additive manufacturing: a comparison between CMT and TopTIG processes applied to stainless steel. *Weld World*. 2018;62:1083–1096.
- [5] Knapp GL, Mukherjee T, Zuback JS, et al. Building blocks for a digital twin of additive manufacturing. *Acta Mater*. 2017;135:390–399.
- [6] Mukherjee T, Manvatkar V, De A, et al. Dimensionless numbers in additive manufacturing. *J Appl Phys*. 2017;121:064904.
- [7] Mukherjee T, DebRoy T. A digital twin for rapid qualification of 3D printed metallic components. *Appl Mater Today*. 2019;14:59–65.
- [8] Xu X, Mi G, Luo Y, et al. Morphologies, microstructures, and mechanical properties of samples produced using laser metal deposition with 316 L stainless steel wire. *Optic Laser Eng*. 2017;94:1–11.
- [9] Chen X, Li J, Cheng X, et al. Microstructure and mechanical properties of the austenitic stainless steel 316L fabricated by gas metal arc additive manufacturing. *Mater Sci Eng: A*. 2017;703:567–577.
- [10] Aref Y, Shamsaei N, Thompson SM, et al. Effects of process time interval and heat treatment on the mechanical and microstructural properties of direct laser deposited 316L stainless steel. *Mater Sci Eng: A*. 2015;644:171–183.

- [11] Gray III GT, Livescu V, Rigg PA, et al. Structure/property (constitutive and spallation response) of additively manufactured 316L stainless steel. *Acta Mater.* 2017;138:140–149.
- [12] Zhang K, Wang S, Liu W, et al. Characterization of stainless steel parts by laser metal deposition shaping. *Mater Des.* 2014;55:104–119.
- [13] Ma M, Wang Z, Zeng X. A comparison on metallurgical behaviors of 316L stainless steel by selective laser melting and laser cladding deposition. *Mater Sci Eng A.* 2017;685:265–273.
- [14] Wang X, Deng D, Yi H, et al. Influences of pulse laser parameters on properties of AISI316L stainless steel thin-walled part by laser material deposition. *Optic Laser Technol.* 2017;92:5–14.
- [15] Bertoli US, Guss G, Wu S, et al. In-situ characterization of laser-powder interaction and cooling rates through high-speed imaging of powder bed fusion additive manufacturing. *Mater Des.* 2017;135:385–396.
- [16] Khairallah SA, Anderson AT, Rubenchik A, et al. Laser powder-bed fusion additive manufacturing: Physics of complex melt flow and formation mechanisms of pores, spatter, and denudation zones. *Acta Mater.* 2016;108:36–45.
- [17] Manvatkar V, De A, DebRoy T. Heat transfer and material flow during laser assisted multi-layer additive manufacturing. *J Appl Phys.* 2014;116(12):124905.
- [18] Caiazzo F, Alfieri V. Laser-aided directed energy deposition of steel powder over flat surfaces and edges. *Materials (Basel).* 2018;11(3):435.
- [19] Mukherjee T, DebRoy T. Mitigation of lack of fusion defects in powder bed fusion additive manufacturing. *J Manuf Process.* 2018;36:442–449.
- [20] Klassen A, Scharowsky T, Körner C. Evaporation model for beam based additive manufacturing using free surface lattice Boltzmann methods. *J Phys D: Appl Phys.* 2014;47(27):275303.
- [21] Szost BA, Terzi S, Martina F, et al. A comparative study of additive manufacturing techniques: residual stress and microstructural analysis of CLAD and WAAM printed Ti-6Al-4V components. *Mater Des.* 2016;89:559–567.
- [22] Yang H, Yang J, Huang W, et al. The printability, microstructure, crystallographic features and microhardness of selective laser melted Inconel 718 thin wall. *Mater Des.* 2018;156:407–418.
- [23] Foroozmehr A, Badrossamay M, Foroozmehr E, et al. Finite element simulation of selective laser melting process considering optical penetration depth of laser in powder bed. *Mater Des.* 2016;89:255–263.
- [24] Mukherjee T, Wei HL, De A, et al. Heat and fluid flow in additive manufacturing—part I: Modeling of powder bed fusion. *Comput Mater Sci.* 2018;150:304–313.
- [25] Ou W, Mukherjee T, Knapp GL, et al. Fusion zone geometries, cooling rates and solidification parameters during wire arc additive manufacturing. *Int J Heat Mass Trans.* 2018;127:1084–1094.
- [26] Manvatkar V, De A, DebRoy T. Spatial variation of melt pool geometry, peak temperature and solidification parameters during laser assisted additive manufacturing process. *Mater Sci Technol.* 2015;31:924–930.
- [27] Mills KC. Recommended values of thermo-physical properties for selected commercial alloys. Cambridge: Woodhead Publishing; 2002.
- [28] Mukherjee T, Zhang W, DebRoy T. An improved prediction of residual stresses and distortion in additive manufacturing. *Comput Mater Sci.* 2017;126:360–372.
- [29] Mukherjee T, Zuback JS, Zhang W, et al. Residual stresses and distortion in additively manufactured compositionally graded and dissimilar joints. *Comput Mater Sci.* 2018;143:325–337.
- [30] Knight CJ. Theoretical modeling of rapid surface vaporization with back pressure. *AIAA J.* 1979;17(5):519–523.
- [31] He X, Fuerschbach P, DebRoy T. Probing temperature during laser spot welding from vapor composition and Modeling. *J Appl Phys.* 2003;94:6949–6958.
- [32] Wang L, Felicelli SD, Pratt P. Residual stresses in LENS-deposited AISI 410 stainless steel plates. *Mater Sci Eng A.* 2008;496:234–241.
- [33] Zhang H, Zhang CH, Wang Q, et al. Effect of Ni content on stainless steel fabricated by laser melting deposition. *Opt Laser Technol.* 2018;101:363–371.
- [34] Li R, Shi Y, Wang Z, et al. Densification behavior of gas and water atomized 316L stainless steel powder during selective laser melting. *Appl Surf Sci.* 2010;256:4350–4356.
- [35] Ding J, Colegrove P, Mehnen J, et al. Thermo-mechanical analysis of wire and arc additive layer manufacturing process on large multi-layer parts. *Comput Mater Sci.* 2011;50(12):3315–3322.